Real-space laser-induced fluorescence imaging applied to gas-liquid interfacial scattering

Title: Real-space laser-induced fluorescence imaging applied to gas-liquid interfacial scattering

Authors: Robert H. Bianchini,[ID] Maksymilian J. Roman,[ID] Matthew L. Costen,[ID] and Kenneth G. McKendrick*[ID]

[ID]ORCID id: Robert H. Bianchini: 0000-0002-3572-8582

[ID]ORCID id: Maksymilian J. Roman: 0000-0002-5113-9470

[ID]ORCID id: Matthew L. Costen: 0000-0002-6491-9812

[ID]ORCID id: Kenneth G. McKendrick: 0000-0001-8979-2195

Affiliation (all authors): Institute of Chemical Sciences, Heriot-Watt University, Edinburgh EH14 4AS, UK

***Contact details: k.g.mckendrick@hw.ac.uk**

Abstract

We describe the real-space imaging of the products of molecular scattering, applied to collisions of hydroxyl radicals with low-vapor-pressure-liquid surfaces. A pulsed molecular beam of OD (for technical reasons) with a mean laboratory-frame kinetic energy of 29.5 kJ mol^{-1} was directed at continually refreshed surfaces of the representative liquids perfluoropolyether, squalane and squalene. Laser-induced fluorescence (LIF) was excited by pulsed laser light shaped into a planar sheet, tuned to selected rovibronic transitions in the OD A-X band. The LIF emission was imaged and intensified before being captured by an external camera. Sequences of images allowed the evolution of the incident packet and scattered plumes of OD molecules to be observed. The results confirm previous observations of the internal-state distributions of the scattered OD and its differential survival probability on different liquid surfaces. New measurements of the angular distributions found them all to be broad and approximately symmetric, independent of the angle of incidence. This is interpreted as implying a high degree of atomic-scale roughness, rather than a predominant trapping-desorption mechanism, because of the other observed signatures of impulsive scattering; these include the degree of OD rotational excitation, superthermal speeds, and the correlation of speed with scattering angle. This approach has considerable potential to be applied in related gas-surface scattering experiments. It is immune from the difficulties of some other imaging methods that involve

charged-particle detection and allows a spatially extended region of the scattering plane perpendicular to the surface to be imaged.

Introduction

Collisions between gas-phase molecules and surfaces are of widespread significance in many fields of scientific and practical interest, including heterogeneous catalysis, gas separation and sequestration, distillation, respiration, among many others. We concentrate here on the gas-liquid interface, which has in general been less well-studied than the corresponding gas-solid interface, but in recent years has been the subject of growing interest.[1-4] In particular, we choose scattering of the hydroxyl radical, OH (or its isotopologue, OD), from liquid surfaces to demonstrate the capabilities of the new technique that we introduce here. These processes are of considerable interest in their own right in the atmosphere, where OH plays a key role in the oxidation of the organic components present at the surfaces of aerosol particles.[5-13]

Information about the mechanisms of the interfacial interactions is encoded in the dynamical properties of the molecules which leave the surface. There is therefore a clear motivation to develop methods capable of measuring the speed, angular, and internal-state distributions of the scattered molecules. A prevailing idea that has emerged from such measurements is the utility of characterising the observations empirically as being combinations of two limiting mechanisms: impulsive scattering (IS), in which the molecules undergo a single, or at most very small number, of ballistic encounters with the surface; and thermal desorption (TD), where the number of encounters is sufficient for the translational and internal degrees of freedom of the scattered molecules to resemble a thermal distribution at the temperature of the liquid.[1-4, 14-18] More detailed investigations suggest caution, however, in interpreting these empirical separations too literally.[19-33] Realistic scattering calculations indicate a range of possibilities, and subtle variations dependent on penetration depth into the liquid, between the limiting extremes.[22-33] This encourages the development of more incisive experimental probes, particularly capable of measuring correlations between the product attributes as we seek to do here, to establish the sensitivities of different observables to the scattering mechanism.

The experimental methods applied in this field to-date have generally involved molecular beams (or, less commonly, laser-photolytically generated) species scattering from continually refreshed surfaces of low-vapor-pressure liquids in vacuum.[4] There have been two broadly distinct approaches to detecting the scattered molecules, based on mass spectrometry and laser spectroscopy, respectively.[3] Mass spectrometric methods[1, 3, 34] have the advantage of being 'universal' and are perhaps most naturally suited to measuring angular and speeds distributions, but they are subject to a number of

limitations. They inherently lack quantum-state resolution. There are also practical restrictions on the measurable range of final angles, particularly in the directly backward direction which is obstructed by the molecular-beam source. Laser-spectroscopic methods are less general, being more specifically suited to particular species in a chosen spectral range; the most widely applied in this field have been laser-induced fluorescence (LIF) to radicals such as OH and NO[19-21, 35-54] and infrared absorption to HF and CO_2.[14-17, 55-60] They do have the inherent advantage of internal-state-resolution, but do not straightforwardly provide speed and angular information without some special effort; partial speed resolution in the direction of propagation of the laser beam is possible by exploiting the Doppler effect.[57, 59]

In gas-phase dynamical scattering measurements, the modern spectroscopic method of choice for measuring state-resolved speed and angular distributions of neutral fragments is to ionise them through resonance-enhanced multiphoton ionization (REMPI),[61] combined with velocity-mapped imaging (VMI) of the ion velocities.[62] REMPI-VMI has been applied effectively in a wide range of gas-phase bimolecular, photodissociation, and photoionization measurements.[63-66] There have been a much smaller number of successful demonstrations of applications to gas-surface scattering.[67-71] There are several limitations that have prevented its more widespread use. The mapped volumes are small, meaning the scattering-angular acceptance is low if it is not close to the surface. A principal problem is then creating the undistorted extraction fields needed for the VMI method, while simultaneously providing access for the incident molecular beam.[71] The difficulties are partially eased if the surface itself is conducting (although this would eliminate many insulating liquids of practical interest) and can effectively be incorporated as the repeller electrode. However, this provides velocity mapping in the plane parallel to the surface, which does not generally coincide with the scattering plane (which contains the surface normal) and is therefore not usually of primary interest.[67, 68] 'Slicing' methods can provide some lower-resolution speed discrimination in the normal direction.[68, 70]

Spatially resolved LIF measurements would therefore appear to be an attractive alternative. One version of this has very recently been demonstrated for NO scattering from liquid surfaces by Zutz and Nesbitt,[54] based on successive pointwise measurements of the LIF intensity emitted from different small volumes of a cylindrical probe beam. However, this is limited in the achievable spatial resolution and requires laborious mechanical movement of the collection optics to map out angular scattering distributions. In addition, in the version reported there was no speed resolution of the scattered products.

An approach in which the whole angular range is captured on each laser pulse would have clear multiplexing advantages. Such planar LIF (pLIF) methods, in which the probe beam is expanded into a

planar sheet and the LIF emission is imaged, are well-established in other fields. They have been widely applied in combustion to map radical densities in flames.[72-76] They have also been used to monitor the evolution of reaction products from catalytic surfaces.[77-80] However, these are much higher density environments, which is presumably one of the main factors that has inhibited their use in molecular-beam scattering experiments. There have been some successful attempts to use LIF-based imaging under the more-rarefied conditions needed to study photodissociation dynamics. These began with the pioneering experiments of McDonald and co-workers using an array of photomultiplier tubes,[81] and continue with sliced-imaging variants and modern array detectors.[82] More recently, other low-density systems have been imaged spatially, including e.g. ultracold species in magneto-optical traps, allowing their temperatures to be assessed.[83]

We introduce here the first successful use of pLIF in gas-liquid scattering, applied to inelastic scattering of OH (or, in practice and as in previous work,[52] OD, to avoid any possible contamination by reactive scattering of OH-producing species) from liquid surfaces. OH scattering from the liquids selected, perfluoropolyether (PFPE), squalane and squalene, has already been partially characterised in other, non-spatially resolved experiments,[19-21] including our recent introduction of a pulsed molecular-beam source of OD.[52] The new development here is to combine this with an imaging system to capture the spatial distribution of the LIF signal excited by a planar probe beam. Variation of the delay between the molecular-beam and probe-laser pulses produces a sequence of images of the ingoing beam and the inelastically scattered plume of OD. We demonstrate proof-of-principle that correlated speed and angular distributions for specific quantum states can be extracted from the images. We consider the new dynamical insight into the scattering mechanism of OD from these prototypical liquid surfaces that a straightforward preliminary analysis already provides.

Experimental

The experimental setup is an extension of that described recently;[52] what follows is a summary of the pre-existing experiment and a more detailed description of the developments introduced here. The apparatus consisted of two stainless-steel chambers, the main scattering chamber and the load-lock chamber, connected *via* a gate valve. A schematic diagram of the main chamber is presented in Figure 1. Vacuum was achieved with turbo pumps backed by scroll pumps (Edwards STP-A1303C backed by Edwards XDS 35i for the main chamber and Edwards STP-301 backed by Edwards XDS 10 for the load-lock chamber). The steady-state background pressure was *ca.* 10^{-6} mbar; this rose to *ca.* 10^{-5} mbar when the molecular-beam valve was operating. These pressures ensured that the mean free path of the molecules in the beam was larger than the distances travelled on their way to the liquid surface (positioned 180.5 ± 0.5 mm from the center of the discharge region), or the shorter distance from the surface back into the observation zone, limiting any gas-phase collisions with background gas.

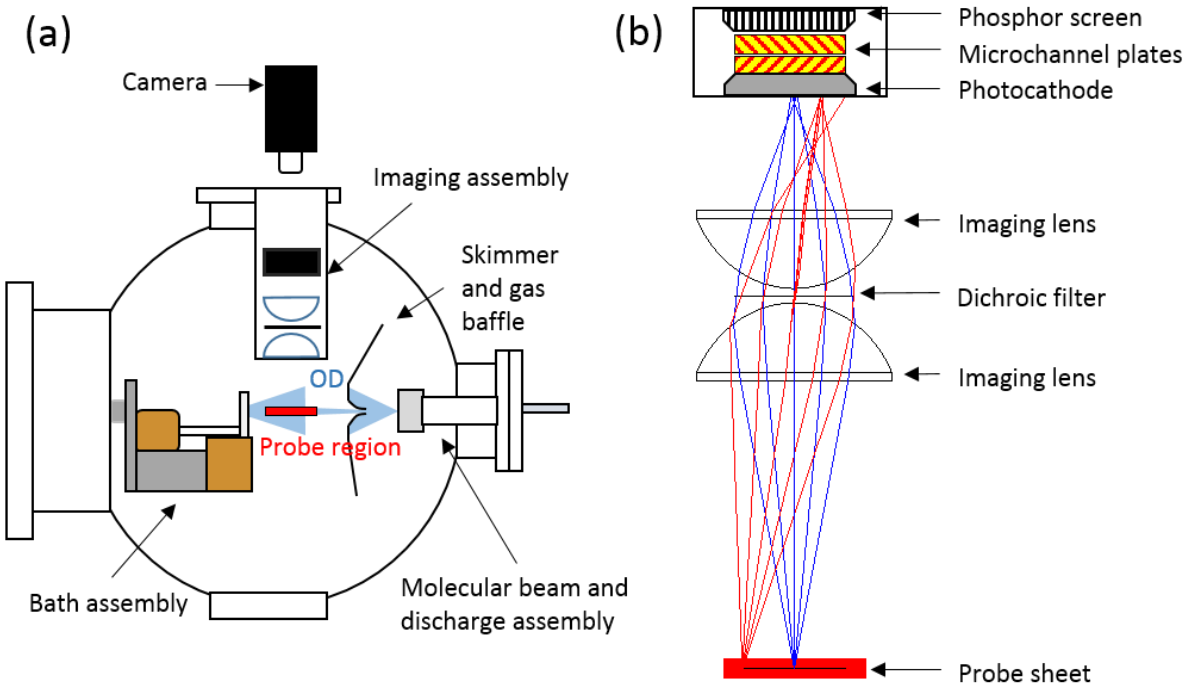

Figure 1: Schematic diagrams of the experimental setup; (a) side view of the main chamber, (b) close up of the imaging assembly.

The molecular beam was created from a mixture of D_2O seeded in He (*ca.* 1% D_2O in 3 bar of He). The gas was introduced into the main chamber through a pulsed valve (General Valve series 9, 1-mm diameter orifice) with a custom-built pulsed high-voltage DC discharge device attached to its faceplate. The firing of the discharge was timed to coincide with the peak of the gas pulse, dissociating

the D_2O and producing OD radicals. The packet of OD radicals had a measured average speed of 1811 ± 8 m s^{-1}, which corresponds to an average laboratory-frame kinetic energy of 29.5 ± 0.3 kJ mol^{-1}. Characterisation of the rotational distributions of the OD in the beam is summarised below, with more details in a previous publication[52] and in the supplementary material. The OD beam was skimmed by a 2-mm skimmer located *ca.* 40 mm from the discharge device. The beam then traversed the region probed by the laser sheet. Two angles of incidence were investigated by physically moving the beam-source assembly: either along the liquid-surface normal (θ_i = 0°) or at 45° to it (θ_i = 45°).

Scattering from the reactive liquids squalane (Sigma-Aldrich, ≥ 99% purity) and squalene (Sigma-Aldrich, ≥ 98% purity) was investigated. PFPE (Krytox® 1506; DuPont) was used as a reference sample, as it has been demonstrated previously to be unreactive and to scatter essentially all of the impinging OD. [19-21, 52] The molecular structures of the liquids are shown in Figure 2.

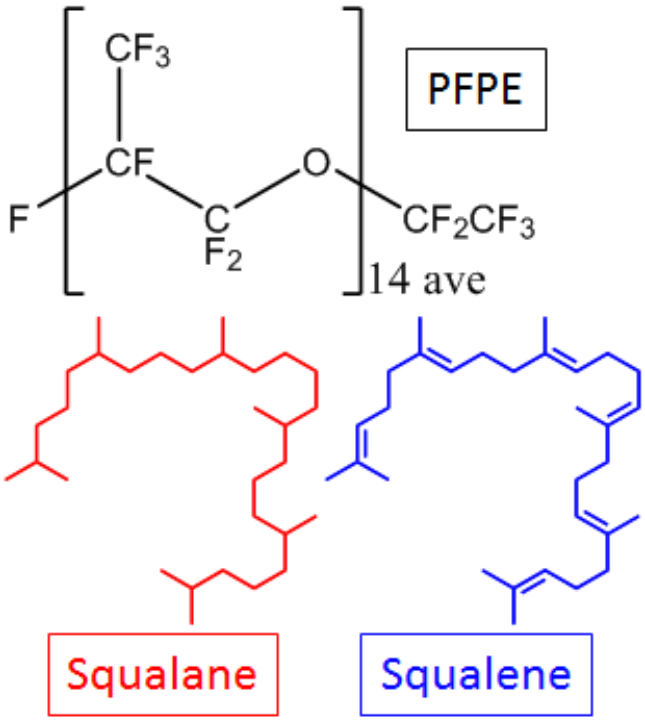

Figure 2: Molecular structures of the liquids studied.

Continually refreshed liquid surfaces were created by rotating at 0.5 Hz a stainless-steel wheel partially submerged in a bath of the chosen liquid. In practice, the wheel-bath assembly consisted of two parallel wheel and bath sets. During measurements, one bath would contain a reactive liquid and the other would contain the reference PFPE. The active surface could be switched between runs by

mechanically translating the baths without having to vent the vacuum system. It was confirmed in separate tests using an alignment laser propagating through the valve body and skimmer that the central point of impact of the molecular beam on each wheel was the same (within ± 1 mm) for both angles of incidence.

OD radicals in $v = 0$ of the ground electronic state were probed on specific rovibronic transitions of the A-X(1,0) band by excitation with tuneable laser light in the range 287-289 nm. The pulsed (~5 ns) probe-laser light was produced by a frequency-doubled dye laser (Sirah Cobra-Stretch, CSTR-LG-24) pumped with the frequency-doubled output (532 nm) of a pulsed Nd:YAG laser (Continuum Surelite II-10). Before entering the main chamber, the laser beam was expanded and subsequently collimated by a pair of cylindrical lenses to produce a sheet. This was *ca.* 4 mm thick and its width was limited to 30 mm by an external iris and the dimensions of the beam-shaping lenses. The longer axis was horizontal in the laboratory, perpendicular to the liquid surface, in the plane containing the incident molecular beam. The distance between the liquid surface and the closer edge of the laser sheet was *ca.* 5 mm.

The spatially resolved observation of the LIF emission was achieved with an image-acquisition setup depicted in more detail in Figure 1(b). The emitted light was collected by a pair of fused silica lenses (Thorlabs La4384, $f = 90.0$ mm) in a telescope arrangement with a magnification of 0.5. A dichroic filter (centred at 317 nm with FWHM = 8 nm, Laser Components) was placed between them to isolate emission on the OD A-X(1,1) band in the 310-313 nm range. The transmitted light was imaged onto an image intensifier (Photek, MCP240/Q/S20/P43/GL), consisting of a photocathode, a chevron stack of microchannel plates (MCPs) and a phosphor screen. A custom-made external unit consisting of a power supply and a gating unit powered the intensifier. The imaged photons ejected primary electrons from the photocathode, which were amplified in the MCPs by a factor of around 10^5 (dependent on applied voltage). The MCPs preserved the signal's spatial distribution. The emerging secondary electrons illuminated the phosphor screen, which was viewed by a CCD camera (Basler Scout FireWire Camera, scA780-54fm) placed outside the main chamber on top of a viewport.

The total intensity of light emitted by the phosphor screen was monitored separately with an avalanche photodiode (SensL, MicroFM10035-X18). LIF excitation spectra were obtained by scanning the laser wavelength at fixed delays between the discharge and the probe laser pulse. These allowed the rotational distributions, integrated across the whole field of view at a given delay, to be characterised.

Spatially resolved images were captured by the camera at selected delays between the firing of the discharge device and the probe laser pulse. Images were 420 x 420 pixels in size, centred on the middle

of the phosphor screen. Other than well-known spectroscopic linestrength factors, the instrument function (i.e. spatial variation in LIF collection efficiency or detector/camera sensitivity), and any motion of the molecules between absorption and emission from the electronically excited state, the intensity of each pixel directly reflects the number density of ground-state OD radicals in the chosen quantum state in the corresponding volume at a particular delay.

We made a preliminary assessment of the instrument function in separate experiments in which the chamber was flooded with a uniform density of OD; this was achieved by running the HV discharge in DC mode and observing pLIF at long discharge-probe delays (> 1 ms). Normalising raw images to this instrument function would have eliminated some relatively minor systematic quantitative variations in signal intensity in the main field of view. However, it also noticeably distorted the images in the marginal regions with low detection sensitivity. The reasons for this are still under investigation. However, we have confirmed that none of the conclusions drawn here from the results below derived from un-normalised images would be materially affected by using the normalised versions.

The blurring effect on the images due to motion of the molecules between absorption and emission can be readily assessed. The radiative lifetime of the relevant rotational levels in $v' = 1$ of the $A^2\Sigma^+$ state is around 750 ns.[84] As noted above, molecules in the in-going beam have a (unidirectional) speed of around 1800 ms^{-1}. Therefore, there is an exponentially decaying smearing effect on the ingoing beam in the direction of travel, with a characteristic distance of around 1.4 mm. This will be closer to 0.8 mm for the scattered molecules, which, as shown below, have peak speeds around ~1,000 ms^{-1}. In either case, this is well below the finite dimensions of the in-going beam (see below), so it does not significantly affect the resolution of the images presented here. In general, this effect could be more important for application of this imaging technique to other molecules with longer radiative lifetimes; however, that could be mitigated if necessary by gating the observed fluorescence.

Most of the noise in raw images results from electronic noise in the camera (see further discussion below). It was discriminated against by applying an intensity threshold to each pixel on each laser shot, below which the intensity was set to zero. The value of the threshold was established empirically by examining the rejection rates for images with and without a significant pLIF signal present. To further improve the signal-to-noise ratio, 500 laser shots were summed to produce a single stored image.

By changing the discharge-probe delay, sequences of images were recorded. These spanned delays of 63 - 143 μs, with a time step of 4 μs, resulting in a total of 21 summed images. Stacking these images produced 'movies' depicting the propagation of the ingoing beam across the probe region and its subsequent scattering from a specific liquid surface. Sequences were recorded on four different transitions: $Q_1(2)$, $Q_1(4)$, $Q_1(6)$ and $Q_1(8)$. For a chosen transition and angle of incidence, each recording

from either of the reactive surfaces was accompanied by an interleaved measurement from PFPE and a separate one with no liquid surface present. Each such set of sequences was repeated three times and the results averaged, from which the desired information on quantum-state-specific angular and speed distributions of the scattered OD was extracted via subsequent offline analysis.

Results

The capabilities of this approach are illustrated in the false-color sequences of real-space pLIF images in Figures 3 and 4 (Multimedia view), for N = 6 with θ_i = 0° and 45°, respectively. A broader survey of scattering from the full range of liquids studied is shown for N = 4, which is closer to the maximum in the scattered rotational distribution, in Figure 5 (with θ_i = 0°) and Figure 6 (θ_i = 45°). Four selected frames are shown in each case.

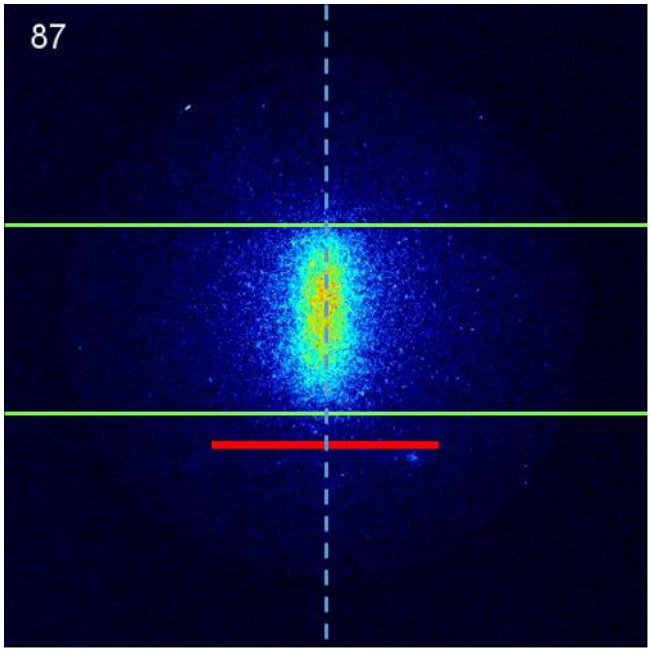

Figure 3: Real-space pLIF imaging of OD N = 6 scattering from PFPE with θ_i = 0°. The images are false-coloured; black indicates an intensity of zero and white indicates the maximum intensity, intermediate intensities are represented progressively on a spectrum from blue to red. The liquid surface is indicated by a red line and lies just below the field of view restricted by the geometry of the probe sheet, the edges of which are denoted approximately by the green lines. In this representation, the sheet propagates from right to left. The dashed blue line is along the surface normal, aligned with the center of the point of impact of the molecular beam with the liquid. The discharge-probe delay in μs is indicated in the top left corner of each frame. (Multimedia view)

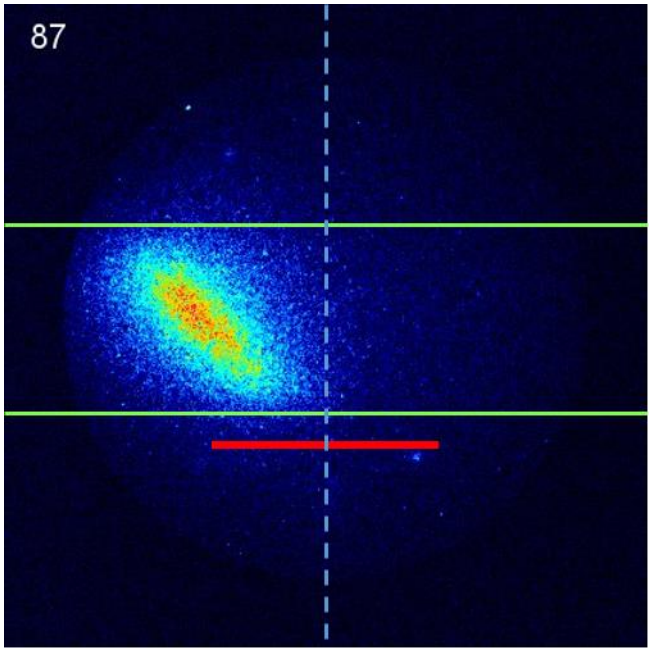

Figure 4: Real-space pLIF imaging of OD N = 6 scattering from PFPE with θ_i = 45°. The false-coloring and the representation of the surface and the laser sheet are the same as in Figure 3. (Multimedia view)

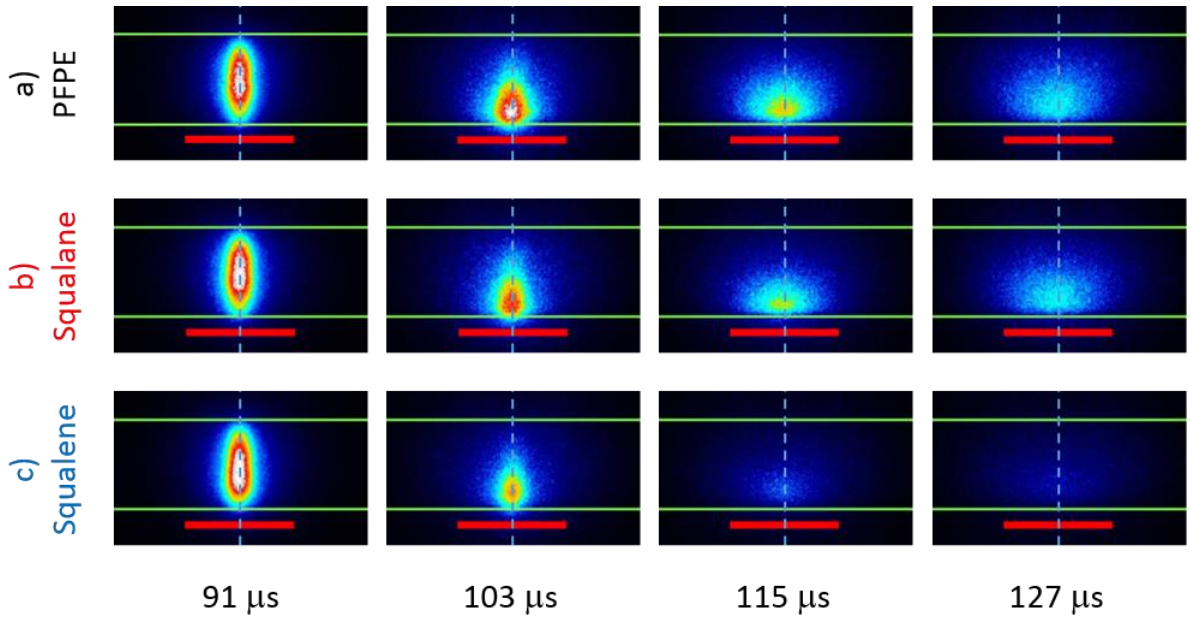

Figure 5: Selected frames from movies of OD in N = 4 scattering from a) PFPE, b) squalane and c) squalene with θ_i = 0°. The discharge-probe delay is indicated underneath each set. The false-coloring and the representation of the surface and the laser sheet are the same as in Figure 3. The sequences

for each liquid have been normalized to the peak intensity of the in-going beam at 91 μs. The three later frames have been amplified by a factor of 3 to enable visual comparison.

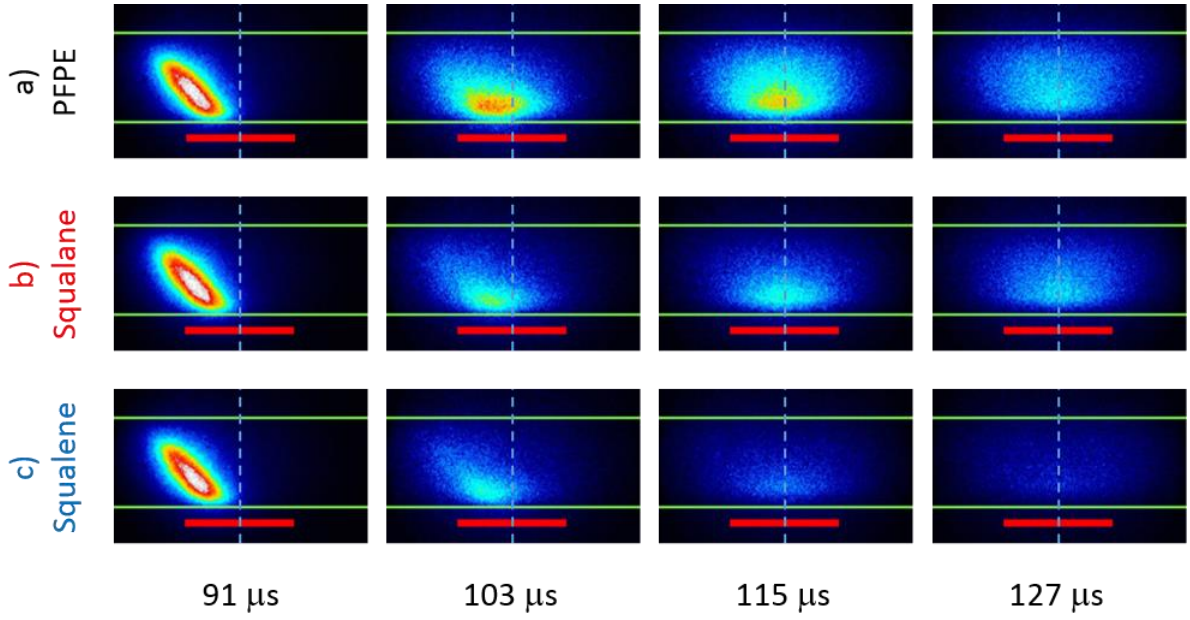

Figure 6: Selected frames from movies of OD in N = 4 scattering from a) PFPE, b) squalane and c) squalene with θ_i = 45°. The discharge-probe delay is indicated underneath each set. The false-coloring and the representation of the surface and the laser sheet are the same as in Figure 3. Normalization of sequences for different liquids is the same as in Fig. 5.

It may be of interest, particularly to assess the potential applicability of this technique in other contexts, to consider the absolute number densities of OD that produce images with the observed signal-to-noise ratios. As explained previously, [52] we estimate a *total* number density at the peak of the molecular beam packet at the point of impact with the surface of order ~2×10^{14} cm^{-3}. The majority of this is He carrier; the D_2O seeding ratio is ~1%, implying a D_2O density of ~2×10^{12} cm^{-3}. The biggest unknown is the fraction of the D_2O that is converted to OD in the discharge. A strict upper bound is obviously 100%; it may in practice be much smaller. This can be used to define an upper limit to the OD density also of ~2×10^{12} cm^{-3}. The largest LIF signals are obtained when probing N = 1 in the in-going beam, which we know constitutes around 50% of the population, implying an upper limit to the number density per quantum state of ~1×10^{12} cm^{-3}.

Individual detected LIF photons are easily distinguishable in single-shot images. They produce an integrated signal of ~ 120 (as measured on an 8-bit digitiser) that is spread over ~3×3 adjacent pixels,

with a peak signal of ~30 per pixel. The average background signal, due to electronic noise in the camera, is 2.0 per pixel, with a standard deviation, σ, of 2.4 per pixel. In comparison, the average integrated signal per laser shot detected when probing $N = 1$ in the vicinity of the peak of the in-going beam is 17 per pixel; this corresponds approximately to a photon overlapping each pixel on every other laser shot. The high-density region corresponding the peak of the molecular beam occupies an area of order ~30×30 pixels.

A commonly adopted working definition of the limit of detection (LOD) is an average signal that is equal to 3σ of the background (equivalent to a ~99.9% one-sided confidence interval for the presence of a signal The upper bound to the LOD, i. e. the number density per quantum state needed to add this level of signal to at least one of the pixels in the peak-density region on a single laser shot, is therefore ~1×10^{12} cm^{-3} / (17 per pixel × 900 pixels / (3 × 2.4)) = ~5×10^{8} cm^{-3}. This can, of course, be reduced in the usual way through signal averaging. For the 500 shots used to obtain single frames of the images in Figs. 3 - 6, the upper bound to the LOD is correspondingly ~2×10^{7} cm^{-3}. At lower count rates, the signal-to-noise could also be improved through established methods of counting events rather than integrating.

Some immediate conclusions can be drawn directly from simple visual inspection of the evolution of the images in Figures 3-6 with delay. The ingoing OD beam can be seen clearly propagating through the probe laser sheet area on its way toward the liquid surface at the expected values of θ_i. Overall, as was obvious from the relative decline in ingoing intensity of the spatial images for higher levels (not shown explicitly), the beam was rotationally cold. This confirmed what was known from earlier single-point detection techniques.[52] It was quantified again here by the excitation spectrum of the beam at its peak intensity, showing that around 70% of the population was in the first two rotational levels, $N = 1$ and 2 (see supplementary material). The new imaging capability allows a more subtle correlation between spatial and internal-state distributions of the ingoing beam to be discerned. The beam is not spatially perfectly uniform, consisting of a predominantly rotationally cold core with warmer edges. This was manifested in the spatial distribution transverse to the direction of propagation, which was symmetric and close to Lorentzian in shape, but with a width that was dependent on rotational level (see supplementary material). We believe, from our preliminary work with different designs of the high-voltage discharge assembly, that this effect may be associated with penetration of the plasma beyond the exit channel of the assembly. The lower density in this region results in a less well-cooled component of the OD population that extends to higher rotational states and with higher off-axis velocities. The spatial distribution in the longitudinal direction of propagation, which is accessible to more conventional single-point techniques,[52] was also reasonably well-described by a Lorentzian

function, but with a longer trailing edge corresponding to slower speeds, which was slightly more pronounced for higher rotational levels.

The scattered plumes are very obvious in all of Figure 3-6. Note that both N = 4 and 6 are very minor fractions of the populations on the ingoing beam. The apparent similarity of the peak number densities in the ingoing beam and scattered plumes is a result of the much broader angular and extended temporal distributions (see below) of the scattered products. Consistent with expectations from previous single-point measurements,[19-21, 52] the ratio of scattered to incident intensities was seen to increase markedly for higher rotational levels. Typical rotational temperatures of ~400 K at the peak of the scattered distribution have been measured previously.[52] The great majority of the outgoing flux in these higher rotational levels must therefore result from inelastic up-scattering of low-N initial levels.

A major feature of Figures 5 and 6 is the variation in the intensity of the integrated scattered OD signal for different liquids. These decline significantly in the sequence PFPE > squalane > squalene. Since the rotational temperatures scattered from different liquids at these collision energies vary only modestly,[52] and the probed level N = 4 is close to the peak of the rotational distribution, these relative intensities almost entirely reflect different probabilities for reactive loss. They are consistent with previous fixed-point measurements of the OH or OD survival probability on these surfaces.[19-21, 52]

One of the primary new insights obtained here is the shape of the scattered plumes. As illustrated in Figs 3 – 6, their transverse widths were considerably larger than those of the ingoing beam. Perhaps more surprisingly, the angular distributions were similarly broad and at least approximately symmetric about the surface normal, regardless of the incident angle. This was true irrespective of the identity of the liquid or the probed transition.

Visual analysis can only provide at best a qualitative sense of the scattered angular distributions. It is even more difficult to assess the speed distributions by eye. A complete analysis would ultimately require a deconvolution of the effects of the spatial and temporal distribution of the incident packet of OD. This has yet to be attempted, but some very insightful initial conclusions can be reached more straightforwardly by analysing the time-dependent variation of integrated intensities in defined regions of interest (ROIs) in sequences of images. This was done here in two distinct ways, designed to highlight different features of the scattering distributions.

The first such approach was to define rectangular ROIs in the scattering plane, located parallel to the liquid surface at a chosen distance and bisected by the surface normal drawn from the center of the point of impact of the incident beams. These ROIs, referred to as “slices”, are shown in Figure 7a

superimposed on a typical scattering image. The slices were chosen to be 30 pixels wide in the direction of the surface normal (*ca.* 5 mm in real space) and had a length corresponding to the visible extent of the scattered plumes. They were centred at *ca.* 8.2, 13.3 and 20.1 mm, respectively, from the position on the images corresponding to the liquid surface, and together covered most of the area of visible scattering. They were labelled according to their proximity to the surface as “near”, “center” or “far”. The intensity profile along each slice was extracted by averaging the intensity from all constituent pixels across its width. Examples can be seen in Figure 7b, which also contains for comparison the corresponding profiles of the incident beam.

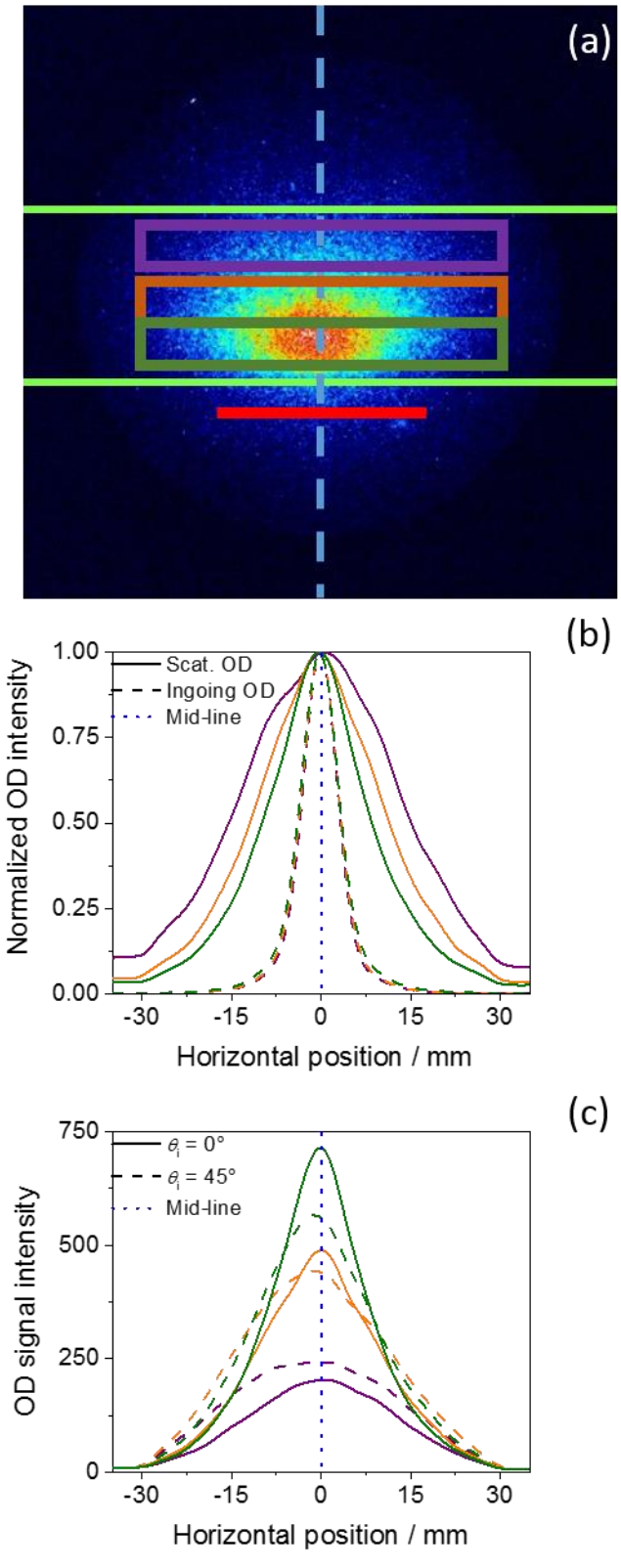

Figure 7: a) Visual representation of the rectangular "slices" used in the intensity-profile analysis, superimposed on an example image of scattered OD (N = 6, scattered from a PFPE surface after approaching it at θ_i = 0°). The slices are color-coded based on their proximity to the liquid surface:

green = “near”, orange = “center”, and purple = “far”. b) Peak-normalized intensity profiles of the ingoing beam (dashed) and the scattered plume (solid) for OD in *N* = 6 approaching a PFPE surface at θ_i = 0°. c) Unnormalized intensity profiles of the scattered plume for OD in *N* = 4 approaching a PFPE surface at θ_i = 0° (solid) and at θ_i = 45° (dashed).

This analysis provided a quantification of the visually obvious much larger and divergent transverse widths of the scattered plumes relative to those of the ingoing beams. The full width at half maximum (FWHM) of the normally incident beam probed on the $Q_1(2)$ transition was 7.1 ± 0.1 mm, extrapolated to the point of impact with the surface. This width remains virtually unchanged across the region of probing, consistent with a well-collimated incident beam. This contrasts with the clear expansion of the scattered signal across the same region (Figure 7b), where the FHWM increases from 19.5, to 23.8, to 29.9 mm for the three respective distances for a normally incident beam. (This corresponds approximately to a plume emerging from a fixed source region only moderately wider (12.3 mm) than the measured FWHM of the ingoing beam, expanding its FWHM linearly at an angle of 24° to the surface normal).

Regardless of the angle of incidence, the chosen liquid surface or the probed transition, the scattered profiles were close to Gaussian in the direction parallel to the surface and peaked very close to the surface normal projecting from the center of the point of impact on the liquid surface. The scattered profiles arising from OD approaching at θ_i = 0° had higher peak intensities and narrower widths than those for θ_i = 45°, as shown in Fig. 7c. This might suggest preferred backwards scattering for θ_i = 0°, concentrating scattering along the surface normal. However, a straightforward analysis (see supplementary material for more details) shows that it can be accounted for simply by the smaller dosed area for θ_i = 0°. The ingoing beam can safely be assumed to be cylindrically symmetric, with the same transverse width for either angle of incidence. For θ_i = 45°, its projection onto the surface was elliptical rather than circular, with a major axis (and also the interaction area) along the scattering plane extended by a factor of $\sqrt{2}$. This in itself is sufficient to account for the observed increased width of the scattered plumes for θ_i = 45°.

As can also be seen in Figure 7c, the integrated intensities in the scattered images decreased with the distance from the liquid surface; this is entirely as expected due to out-of-plane scattering leading to escape from the probe sheet of finite (*ca.* 4 mm) thickness. For collisions at normal incidence, the relative peak heights and total integrated intensities of the probed scattered plume were shown to decrease in a way that was quantitatively consistent (see supplementary material) with a cylindrically

symmetric scattering plume expanding equally in the observed plane and in the unobserved plane perpendicular to it.

The second of the two data-processing approaches used here was designed to generate time-of-flight (TOF) profiles for small individual ROIs distributed across the image. Square ROIs of 10 x 10 pixels (*ca.* 1.7 x 1.7 mm) were placed along radii at five final angles (θ_f = -45°, -22.5°, 0°, 22.5° and 45° with respect to the surface normal drawn from the central point of impact of the incident beams, where negative angles represent scattering to the side (left as shown) from which the 45° beam was incident) and at five radial distances from the surface (d = 7.7, 10.2, 13.6, 17.0 and 21.3 mm respectively). Figure 8 shows the positions of some of the ROIs superimposed on an image of ingoing and scattered OD radicals. The integrated signal intensity within the ROIs as a function of discharge-probe delay yielded the OD TOF profiles.

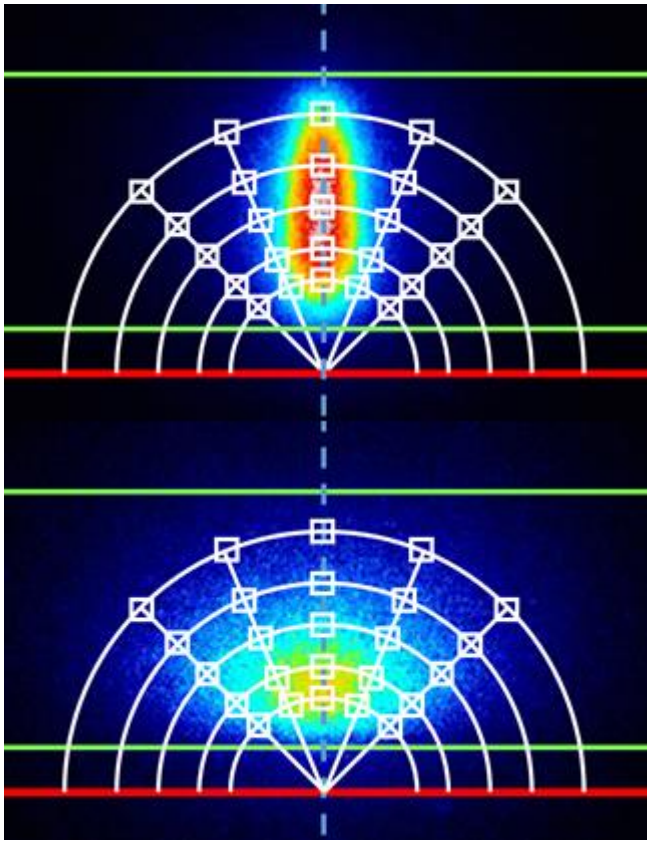

Figure 8: Representations of the square ROIs used in the analysis of TOF profiles superimposed on an example image of a) incident and b) scattered OD. The white arcs represent the five distances: 7.7, 10.2, 13.6, 17.0 and 21.3 mm from the center of the point of impact on the liquid surface (indicated by the red line). The white radial lines indicate the five angles of scattering: -45°, -22.5°, 0°, 22.5° and 45° respectively from left to right.

As shown in the example in Figure 9, both the ingoing beam (sharp peak at early delays) and scattered molecules (long tail at late delays) were present in the profiles, as of course expected. To isolate the scattered component, TOF profiles with the liquid surface retracted from the chamber were subtracted from the respective profiles with the liquid surface present. The long-term stability of the experimental conditions was not sufficient for the relative intensities in these independent measurements to be completely reliable. Therefore, the ingoing beam profiles were scaled in such a way, that upon their subtraction from the total profiles, the resultant scattered OD profiles would have an intensity of zero at the delay of 99 μs; this was chosen as the latest point at which no significant scattered signal should yet have entered the probed region. The adjustments were typically between ±5-10% of the peak signal intensity, but were found to vary with the scattering angle, distance from the surface and the probed transition. Imperfections in this subtraction resulted in some degree of residual physically impossible negative and artificially positive signal intensities at delays earlier than 99 μs. Figure 9 illustrates the subtraction process. For most rotational levels these effects were assessed to be relatively negligible in the region of the peaks in the subtracted profiles used in the subsequent analysis. However, for $Q_1(2)$, reflecting the much larger ingoing contribution in low *N*, the residual scattered OD signal was deemed to not be sufficiently reliable for further analysis.

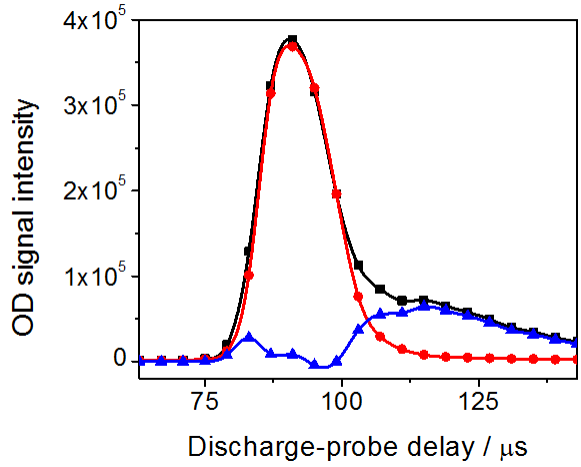

Figure 9: Example of TOF profile of OD intensity passing through a 10 x 10 pixel ROI located 17 mm from the surface and at θ_f = 0°. OD in *N* = 4 travelling initially at normal incidence. The black line is the TOF profile measured with a PFPE surface in the chamber. The red line represents a profile measured without any surface. This profile was scaled to match the black profile at the delay of 99 μs. The blue line represents the subtraction and hence isolates the TOF profile of the scattered OD.

The resultant scattered OD profiles were fitted to the empirical function

$$I(t) = Aexp\left[1 - exp\left[-\left(\frac{t-t_c}{w}\right)\right] - \left(\frac{t-t_c}{w}\right)\right] \qquad \textbf{(1)}$$

where *A* is the peak amplitude and *w* is a width parameter, to find the peak arrival time, t_c, of the scattered OD signal, *I*(t), in a given ROI. This was then used to determine the speed of propagation of the peak signal as a function of final angle. Figure 10 shows TOF profiles that illustrate the progression of the normally incident ingoing beam's and scattered signal's peak arrival times in five ROIs placed along θ_f = 0°. Plots of the peak times against the respective distances from the surface were found to be linear, as would be expected, with slopes corresponding to the inverse of the OD peak speeds. Figure 11 shows the results of this process for an ingoing beam and the OD scattered from the three different liquid surfaces.

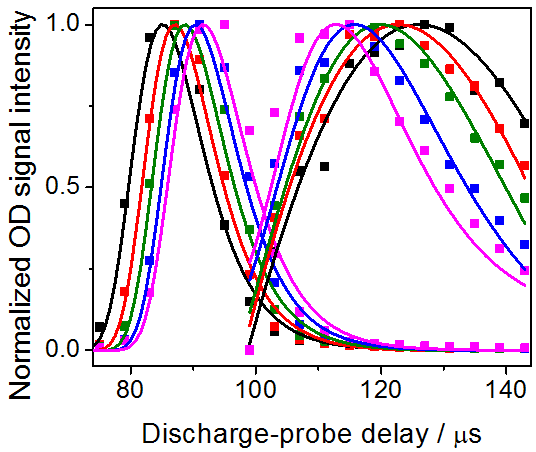

Figure 10: Comparison of the normalized intensity of the ingoing beam of OD (sharp peaks at early delays) and OD scattered off a PFPE surface (broader peaks at later delays). OD in *N* = 4 travelling at θ_i and θ_f = 0°, respectively, through ROIs located at 7.7 (magenta), 10.2 (blue), 13.6 (green), 17.0 (red) and 21.3 mm (black) from the center of the point of impact . The solid lines are the fits to equation (1).

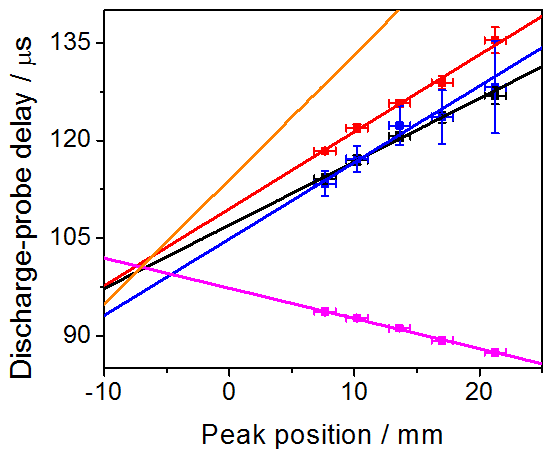

Figure 11: Peak times in TOF profiles for OD N = 4 against distance of the corresponding ROI along the normal from the center of the point of impact. Incident beam with θ_i = 0° (magenta) and scattered from PFPE (black), squalane (red), and squalene (blue). The orange line corresponds, for comparison, to the most probable thermal (300 K) speed of 522 ms^{-1}.

Discussion

Although the primary focus here has been on the demonstration of the technical capabilities of the new method, which has been achieved successfully, we reflect relatively briefly on what dynamical information on OD gas-liquid scattering these first observations contain. As described in the Introduction, it has been common in this field to characterise product distributions in terms of limiting IS and TD mechanisms, both for the internal, particularly rotational, states of the products, [14-17, 53-60] and translational energy and angular distributions. [1, 3, 34] It is known from previous work using single-point detection[19-21, 52] that a significant component of the OD (or OH) scattered at the relevant moderately superthermal energies from the liquids studied here has some distinct 'IS' characteristics: the products are rotationally hotter than the temperature of the liquid and their average speeds are also higher than the thermal average at the liquid temperature.

We confirm both of these features here. The relative intensities of images taken on different probe transitions reflect significant impulsive translational-to-rotational (T-R) energy transfer, populating levels up to at least N = 8. The apparent product speeds are also higher than thermal: an example of this can be seen in Fig. 11, where the most probable speed for a thermal distribution at the liquid temperature (520 ms^{-1}) is contrasted with the considerably higher observed phenomenological speeds of propagation of the peak in the outgoing waves of scattered OD. These speeds are in the region of 1,000 ms^{-1} for recoil along the normal for all three liquids. Some caution is probably appropriate to avoid potential over-interpretation of these absolute values, because a more rigorous analysis should take account of a density-flux transformation, not achievable in any straightforward way because of the non-negligible temporal spread of the incident packet, and the geometric effects of its finite transverse width. These effects may account for the observation that the extrapolated lines for the ingoing and scattered OD in Fig. 11 do not intersect at the known location of the surface, as otherwise should be expected, because they would both result in peak arrival times that are shifted to later times. To a first approximation, the true most-probable scattered speeds should in that case be *higher* than concluded here. Furthermore, there are systematic differences between the phenomenological speeds for the different liquids, also seen previously,[52] that immediately rule out a dominant simple TD mechanism. This does not exclude the possibility that a fraction of the slower molecules in low-to-medium N levels might be assigned to the TD component in a formal phenomenological IS: TD binary separation, but it is clear that much of the observed scattering is better-described as impulsive.

The new capabilities introduced here allow us to assess what angle-resolved measurements might reveal about the scattering mechanism. Considering first the simple probability of scattering as a function of angle (visually assessible in Figures 3-7), there is a distinct lack of any clear preference for

specular scattering. This was confirmed in the ROI analysis. Whether any of the observed distributions fit quantitatively to the $\cos\theta_f$ dependence expected for a TD process would require a more refined analysis in which the geometric averaging over the current significant transverse spread was included. However, the main point is that quite generally the distributions are broad and at least approximately left-right symmetric, regardless of liquid, product rotational state, or, most tellingly, angle of incidence. There are at most subtle differences in the distributions for θ_i = 0° or θ_i = 45°, as can be seen directly from Figure 3 versus Figure 4, Figure 5 versus Figure 6, or Figure 7c. As noted, any subtle differences may be accounted for by simple geometric factors relating to differences in the dosed area of the surface (see above and the supplementary material).

These broad distributions may at first sight seem surprising; a propensity for near-specular scattering is obviously the expected result if the liquid surface appears 'flat' to the OD projectiles. Such a preference has been seen in some related gas-liquid scattering experiments, but it tends to be pronounced only for quite shallow, near-grazing angles (typically θ_i = 60°) and for relatively high initial kinetic energies.[34, 85-89] For θ_i = 45° and below, it has been known since the early experiments on noble gas scattering from liquids such as PFPE and squalane (as also studied here) that the distributions are much broader with no strong preference for forward scattering.[85, 90] As noted in the Introduction, it was generally not possible in those molecular-beam-based experiments to assess the full angular range of final angles and hence the true degree of asymmetry about the surface normal. In the more recent pointwise LIF measurements on NO scattering from these and related liquids by Zutz and Nesbitt, there was no asymmetry in the angular distributions at lower collision energies (11 kJ mol^{-1}).[54] At much higher energies, asymmetry began to emerge, but only in the higher rotational states that must be the result of strongly impulsive collisions inducing T-R energy transfer. The most closely related theoretical predictions to the current work are the trajectory calculations of Troya.[33] These were designed to simulate the conditions of our own original photolytically initiated OH + liquid scattering experiments.[19-21] For computational reasons, the surface in Troya's QCT calculations was taken to be a model fluorinated self-assembled monolayer (SAM) surface. This has been argued, there and in other work, to be a reasonable proxy for a PFPE surface.[29, 33, 58] The QCT calculations predicted OH angular distributions, which at that time had not yet been observed, that were very broad and independent of the final quantum state. These predictions hence correctly anticipated, at least qualitatively, the new results we have now obtained here.

The clear implication of these broad angular distributions, as originally concluded by Nathanson, Minton and subsequently others,[1, 34, 54, 85, 86, 91-93] is that these liquid surfaces appear to the incoming projectiles as being considerably rough on an atomic scale, especially at relatively low-kinetic energies. This leads to scattering into a wide range of final angles even in an IS impulsive scattering mechanism.

This is consistent with molecular dynamics simulations of the surface structure, which predict a substantial level of molecular-level roughness in these liquids at the relevant ambient temperatures.[21, 27, 29, 33, 94, 95] These ideas extend to molecular scattering from related condensed-phase surfaces, e.g. in recent simulations of O_2 collisions with perfluorosulfonic acid ionomer thin films.[96]

The further question then arises whether any signature of the impulsive scattering process remains in the angle-resolved measurements? The answer is yes, when the full capability to resolve *correlated* speed and angular distributions is exploited. The ROI analysis illustrated in Figures 8-11 returns peak product speeds as a function of scattering angle, θ_f. The full results are tabulated in the supplementary material for all three liquids for θ_f spanning the range from -45°to +45°, for N = 4, 6 and 8, and for θ_i = 0° or θ_i = 45°, respectively. Representative examples are plotted for N = 4 with θ_i = 0° in Figure 12(a). These results reinforce the systematic differences in absolute speeds for different liquids noted above. These are most straightforwardly interpreted in terms of expected differences in liquid 'stiffness', with collisions with PFPE being significantly more elastic than with the hydrocarbon liquids.[14, 85, 93, 97, 98] More importantly, the data provide the first evidence that there are clear correlations between the peak OD speed and scattering angle. Figure 12(a) reveals an approximately symmetric (as is required for θ_i = 0°) increase in product speed with the absolute magnitude of $|\theta_f|$. Even more strikingly, for θ_i = 45° in Figure 12(b), the product speeds increase monotonically from θ_f = -45°to +45°. A direct comparison between the contrasting final-angle-dependent absolute speeds at the two different angles of incidence is provided in the construction in Figure 13, for the example of PFPE.

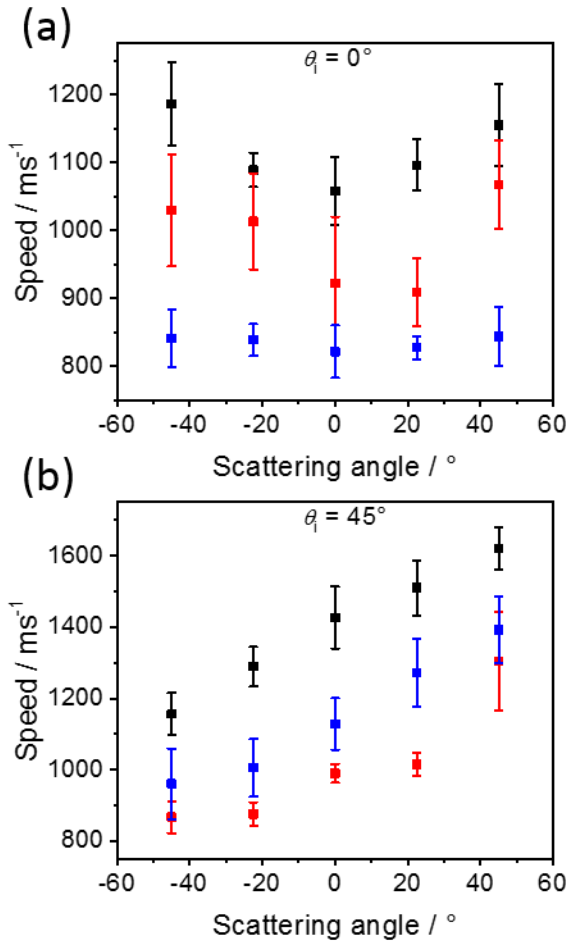

Figure 12: Peak speeds of OD *N* = 4 radicals scattered from PFPE (black), squalane (red) and squalene (blue) liquid surfaces as a function of scattering angle for OD approaching the surface at (a) θ_i = 0° and (b) θ_i = 45°.

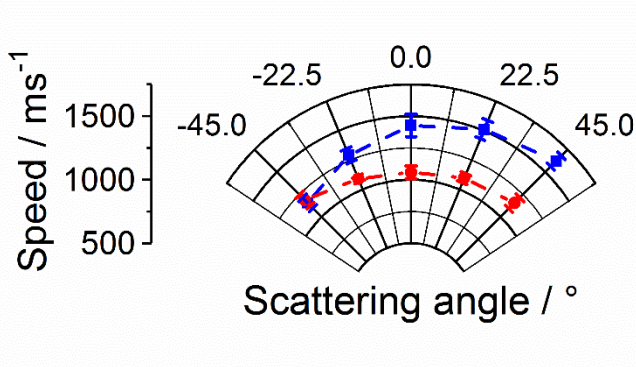

Figure 13: Comparison between final-angle-dependent peak speeds of OD *N* = 4 scattered from PFPE for θ_i = 0° (red) and θ_i = 45° (blue).

These new observations are at least qualitatively consistent with established impulsive 'hard-sphere' models of gas-liquid scattering, in which the surface is treated as a single finite mass.[1, 3, 34, 86, 93] The momentum transferred to the surface is then a simple closed-form function of the deflection angle, χ, defined as 180° - (θ_i + θ_f), and not of θ_i and θ_f separately. The model can be refined to include additional inelastic loss to internal motions of the surface (or projectile).[3, 93] Either version predicts that the minimum product speed should be observed for χ = 180°, i.e. backward scattering. This is true here, as shown in Figures 11 and, more clearly, 12. As can be seen in these Figures, and also most directly in Figure 13, there is fairly good absolute agreement between both the χ = 180° results (i.e. θ_i = 0°, θ_f = 0°, and θ_i = 45°, θ_f = -45°, as defined here). However, this does not appear to extend over the full range of χ, with a weaker dependence on θ_f for θ_i = 0° than would be required to match that for θ_i = 45°. Whether this is a genuine effect, or simply an artefact of the current relatively simple level of analysis, remains to be established. Nevertheless, the existence of strong correlations of the type expected for impulsive scattering seems beyond doubt.

Conclusion

The application of planar-laser-induced-fluorescence imaging to gas-surface scattering has been demonstrated successfully for the first time. State-resolved scattering of moderately superthermal OD molecules from low-vapor-pressure liquids has been observed. New information was provided on the correlated speed and angular distributions, extracted through straightforward analyses of the spatial variation of signal intensity in sequences of images. This shows that the existence of broad and symmetric angular distributions, independent of the angle of incidence, is not in itself good evidence for a predominant trapping-desorption mechanism. Other features of the dynamics, including the degree of rotational excitation, superthermal speeds, and their correlation with scattering angle, all imply a substantial component of impulsive scattering.

This approach has considerable potential to provide dynamical information in scattering experiments for a wide variety of molecules that are detectable by LIF. We estimate an upper bound to the limit of detection (number density of molecules per quantum state needed to produce a signal discernible above the variation in the background in at least one pixel of the image) on a single laser shot of ~5 × 10^8 cm^{-3}; this may be smaller in practice if the efficiency of OD production is lower than assumed, and can obviously be improved through signal averaging or other established data-processing techniques. The method is not confined to gas-liquid scattering, being equally applicable to scattering from solid surfaces. Unlike some other methods, it is not constrained by the electrical properties of the surface and does not require intrusive grids or electrodes. It provides speed and angular information in the

scattering plane perpendicular to the surface; is not confined to detection in a small 'mapping' volume; and is not constrained geometrically from detecting backscattering in the direction of the incident molecular beam. It can also be extended, in principle, to the simultaneous determination of the anisotropy of the rotational angular momentum vectors of the scattered products. As for other forms of optical spectroscopy, this is achievable using polarized light, including e.g. polarized infrared absorption that has already been applied to CO_2 collisions with liquid surfaces.[60]

Supplementary Material

See supplementary material for S1: characterisation of the OD molecular beam; S2: transverse profiles of the ingoing beam for different OD rotational levels; S3: geometric effects of different angles of incidence on the width of the scattered plume at; S4: extent of out-of-plane scattering; S5: rotational-level-dependent peak product speeds for different liquids as a function of incident and final angles.

Acknowledgments

We are grateful to Grant Paterson and Matthew Bain for contributions to the design and commissioning of the apparatus. We thank Alan Greenaway and David Lee (UK Astronomy Technology Centre) for modelling the performance of the light-collection optics. Vanessa Tang assisted with the collection of some of the data presented here.

We acknowledge funding from UK EPSRC (grants EP/G029601/1 and EP/P001459/1; and DTP studentship for MJR) and Heriot-Watt University (James Watt Scholarship for RHB).

References

1 G. M. Nathanson, Annu. Rev. Phys. Chem. **55**, 231 (2004).

2 P. Davidovits, C. E. Kolb, L. R. Williams, J. T. Jayne, and D. R. Worsnop, Chem. Rev. **106**, 1323 (2006).

3 M. A. Tesa-Serrate, E. J. Smoll, T. K. Minton, and K. G. McKendrick, Annu. Rev. Phys. Chem. **67**, 515 (2016).

4 J. A. Faust, and G. M. Nathanson, Chem. Soc. Rev. **45**, 3609 (2016).

5 G. B. Ellison, A. F. Tuck, and V. Vaida, J. Geophys. Res.: Atmos. **104**, 11633 (1999).

6 Y. Rudich, Chem. Rev. **103**, 5097 (2003).

7 D. J. Donaldson, and V. Vaida, Chem. Rev. **106**, 1445 (2006).

8 B. J. Finlayson-Pitts, Phys. Chem. Chem. Phys. **11**, 7760 (2009).

9 D. L. Che, J. D. Smith, S. R. Leone, M. Ahmed, and K. R. Wilson, Phys. Chem. Chem. Phys. **11**, 7885 (2009).

10 J. D. Smith, J. H. Kroll, C. D. Cappa, D. L. Che, C. L. Liu, M. Ahmed, S. R. Leone, D. R. Worsnop, and K. R. Wilson, Atmos. Chem. Phys. **9**, 3209 (2009).

11 F. A. Houle, W. D. Hinsberg, and K. R. Wilson, Phys. Chem. Chem. Phys. **17**, 4412 (2015).

12 R. C. Chapleski, Y. Zhang, D. Troya, and J. R. Morris, Chem. Soc. Rev. **45**, 3731 (2016).

13 S. Enami, Y. Sakamoto, K. Hara, K. Osada, M. R. Hoffmann, and A. J. Colussi, Environ. Sci. Technol. **50**, 1834 (2016).

14 B. G. Perkins, Jr., and D. J. Nesbitt, J. Phys. Chem. B **110**, 17126 (2006).

15 A. M. Zolot, W. W. Harper, B. G. Perkins, P. J. Dagdigian, and D. J. Nesbitt, J. Chem. Phys. **125**, 021101 (2006).

16 B. G. Perkins, Jr., and D. J. Nesbitt, J. Phys. Chem. A **111**, 7420 (2007).

17 B. G. Perkins, Jr., and D. J. Nesbitt, J. Phys. Chem. B **112**, 507 (2008).

18 A. W. Gisler, and D. J. Nesbitt, Faraday Discuss. **157**, 297 (2012).

19 P. A. J. Bagot, C. Waring, M. L. Costen, and K. G. McKendrick, J. Phys. Chem. C **112**, 10868 (2008).

20 C. Waring, K. L. King, P. A. J. Bagot, M. L. Costen, and K. G. McKendrick, Phys. Chem. Chem. Phys. **13**, 8457 (2011).

21 K. L. King, G. Paterson, G. E. Rossi, M. Iljina, R. E. Westacott, M. L. Costen, and K. G. McKendrick, Phys. Chem. Chem. Phys. **15**, 12852 (2013).

22 S. B. M. Bosio, and W. L. Hase, J. Chem. Phys. **107**, 9677 (1997).

23 T. Y. Yan, W. L. Hase, and J. R. Barker, Chem. Phys. Lett. **329**, 84 (2000).

24 T. Y. Yan, and W. L. Hase, J. Phys. Chem. B **106**, 8029 (2002).

25 T. Y. Yan, N. Isa, K. D. Gibson, S. J. Sibener, and W. L. Hase, J. Phys. Chem. A **107**, 10600 (2003).

26 N. Isa, K. D. Gibson, T. Yan, W. Hase, and S. J. Sibener, J. Chem. Phys. **120**, 2417 (2004).

27 E. Martinez-Nunez, A. Rahaman, and W. L. Hase, J. Phys. Chem. C **111**, 354 (2007).

28 Y. X. Peng, L. Liu, Z. Cao, S. Li, O. A. Mazyar, W. L. Hase, and T. Y. Yan, J. Phys. Chem. C **112**, 20340 (2008).

29 J. J. Nogueira, S. A. Vazquez, U. Lourderaj, W. L. Hase, and E. Martinez-Nunez, J. Phys. Chem. C **114**, 18455 (2010).

30 D. Troya, and G. C. Schatz, J. Chem. Phys. **120**, 7696 (2004).

31 B. Scott Day, J. R. Morris, and D. Troya, J. Chem. Phys. **122**, 214712 (2005).

32 J. P. Layfield, and D. Troya, J. Chem. Phys. **132**, 134307 (2010).

33 D. Troya, Theor. Chem. Acc. **131**, 1072 (2012).

34 D. J. Garton, T. K. Minton, M. Alagia, N. Balucani, P. Casavecchia, and G. G. Volpi, Faraday Discuss. **108**, 387 (1997).

35 F. Ausfelder, and K. G. McKendrick, Prog. React. Kinet. Mech. **25**, 299 (2000).

36 H. Kelso, S. P. K. Kohler, D. A. Henderson, and K. G. McKendrick, J. Chem. Phys. **119**, 9985 (2003).

37 S. P. K. Kohler, M. Allan, H. Kelso, D. A. Henderson, and K. G. McKendrick, J. Chem. Phys. **122**, 024712 (2005).

38 S. P. K. Kohler, M. Allan, M. L. Costen, and K. G. McKendrick, J. Phys. Chem. B **110**, 2771 (2006).

39 M. Allan, P. A. J. Bagot, M. L. Costen, and K. G. McKendrick, J. Phys. Chem. C **111**, 14833 (2007).

40 M. Allan, P. A. J. Bagot, S. P. K. Koehler, S. K. Reed, R. E. Westacott, M. L. Costen, and K. G. McKendrick, Phys. Scr. **76**, C42 (2007).

41 M. Allan, P. A. J. Bagot, R. E. Westacott, M. L. Costen, and K. G. McKendrick, J. Phys. Chem. C **112**, 1524 (2008).

42 C. Waring, P. A. J. Bagot, M. T. Raeisaenen, M. L. Costen, and K. G. McKendrick, J. Phys. Chem. A **113**, 4320 (2009).

43 C. Waring, P. A. J. Bagot, M. W. P. Bebbington, M. T. Raisanen, M. Buck, M. L. Costen, and K. G. McKendrick, J. Phys. Chem. Lett. **1**, 1917 (2010).

44 C. Waring, P. A. J. Bagot, J. M. Slattery, M. L. Costen, and K. G. McKendrick, J. Phys. Chem. Lett. **1**, 429 (2010).

45 C. Waring, P. A. J. Bagot, J. M. Slattery, M. L. Costen, and K. G. McKendrick, J. Phys. Chem. A **114**, 4896 (2010).

46 C. Waring, P. A. J. Bagot, M. L. Costen, and K. G. McKendrick, J. Phys. Chem. Lett. **2**, 12 (2011).

47 C. Waring, K. L. King, M. L. Costen, and K. G. McKendrick, J. Phys. Chem. A **115**, 7210 (2011).

48 M. A. Tesa-Serrate, K. L. King, G. Paterson, M. L. Costen, and K. G. McKendrick, Phys. Chem. Chem. Phys. **16**, 173 (2014).

49 M. A. Tesa-Serrate, B. C. Marshall, E. J. Smoll, S. M. Purcell, M. L. Costen, J. M. Slattery, T. K. Minton, and K. G. McKendrick, J. Phys. Chem. C **119**, 5491 (2015).

50 S. M. Purcell, M. A. Tesa-Serrate, B. C. Marshall, D. W. Bruce, L. D'Andrea, M. L. Costen, J. M. Slattery, E. J. Smoll, T. K. Minton, and K. G. McKendrick, Langmuir **32**, 9938 (2016).

51 M. A. Tesa-Serrate, E. J. Smoll, L. D'Andrea, S. M. Purcell, M. L. Costen, D. W. Bruce, J. M. Slattery, T. K. Minton, and K. G. McKendrick, J. Phys. Chem. C **120**, 27369 (2016).

52 R. H. Bianchini, M. A. Tesa-Serrate, M. L. Costen, and K. G. McKendrick, J. Phys. Chem. C **122**, 6648 (2018).

53 M. P. Ziemkiewich, A. Zutz, and D. J. Nesbitt, J. Phys. Chem. C **116**, 14284 (2012).

54 A. Zutz, and D. J. Nesbitt, J. Chem. Phys. **147**, 054704 (2017).

55 W. B. Chapman, B. W. Blackmon, S. Nizkorodov, and D. J. Nesbitt, J. Chem. Phys. **109**, 9306 (1998).

56 B. G. Perkins, T. Haber, and D. J. Nesbitt, J. Phys. Chem. B **109**, 16396 (2005).

57 A. M. Zolot, P. J. Dagdigian, and D. J. Nesbitt, J. Chem. Phys. **129**, 194705 (2008).

58 J. J. Nogueira, S. A. Vazquez, O. A. Mazyar, W. L. Hase, B. G. Perkins, Jr., D. J. Nesbitt, and E. Martinez-Nunez, J. Phys. Chem. A **113**, 3850 (2009).

59 B. G. Perkins, and D. J. Nesbitt, Phys. Chem. Chem. Phys. **12**, 14294 (2010).

60 B. G. Perkins, and D. J. Nesbitt, J. Phys. Chem. A **114**, 1398 (2010).

61 D. W. Chandler, and P. L. Houston, J. Chem. Phys. **87**, 1445 (1987).

62 A. Eppink, and D. H. Parker, Rev. Sci. Instrum. **68**, 3477 (1997).

63 M. N. R. Ashfold, N. H. Nahler, A. J. Orr-Ewing, O. P. J. Vieuxmaire, R. L. Toomes, T. N. Kitsopoulos, I. A. Garcia, D. A. Chestakov, S. M. Wu, and D. H. Parker, Phys. Chem. Chem. Phys. **8**, 26 (2006).

64 A. I. Chichinin, K. H. Gericke, S. Kauczok, and C. Maul, Int. Rev. Phys. Chem. **28**, 607 (2009).

65 D. W. Chandler, P. L. Houston, and D. H. Parker, J. Chem. Phys. **147**, 013601 (2017).

66 A. G. Suits, Rev. Sci. Instrum. **89**, 111101 (2018).

67 S. P. K. Koehler, Y. Y. Ji, D. J. Auerbach, and A. M. Wodtke, Phys. Chem. Chem. Phys. **11**, 7540 (2009).

68 J. R. Roscioli, and D. J. Nesbitt, Faraday Discuss. **150** (2011).

69 M. Reid, and S. P. K. Koehler, Rev. Sci. Instrum. **84**, 044101 (2013).

70 D. J. Harding, J. Neugebohren, D. J. Auerbach, T. N. Kitsopoulos, and A. M. Wodtke, J. Phys. Chem. A **119**, 12255 (2015).

71 D. J. Hadden, T. M. Messider, J. G. Leng, and S. J. Greaves, Rev. Sci. Instrum. **87**, 106104 (2016).

72 M. J. Dyer, and D. R. Crosley, Opt. Lett. **7**, 382 (1982).

73 G. Kychakoff, R. D. Howe, R. K. Hanson, and J. C. McDaniel, Appl. Opt. **21**, 3225 (1982).

74 K. Kohsehoinghaus, Prog. Energy Combust. Sci. **20**, 203 (1994).

75 A. C. Eckbreth, *Laser diagnostics for combustion temperature and species* (Gordon & Breach, Amsterdam ; United Kingdom, 1996), 2nd edn.,

76 M. Alden, J. Bood, Z. S. Li, and M. Richter, Proc. Combust. Inst. **33**, 69 (2011).

77 E. Fridell, U. Westblom, M. Alden, and A. Rosen, J. Catal. **128**, 92 (1991).

78 F. Gudmundson, E. Fridell, A. Rosen, and B. Kasemo, J. Phys. Chem. **97**, 12828 (1993).

79 S. Blomberg, J. F. Zhou, J. Gustafson, J. Zetterberg, and E. Lundgren, J. Phys.: Condens. Matter **28**, 453002, 453002 (2016).

80 J. Zetterberg, S. Blomberg, J. F. Zhou, J. Gustafson, and E. Lundgren, in *Operando Research in Heterogeneous Catalysis*, edited by J. Frenken, and I. Groot (Springer International Publishing Ag, Cham, 2017), pp. 131.

81 D. Eres, M. Gurnick, and J. D. McDonald, J. Chem. Phys. **81**, 5552 (1984).

82 Y. W. Chen, T. H. Yang, and K. M. Chen, Phys. Chem. Chem. Phys. **11**, 7111 (2009).

83 A. L. Collopy, S. Q. Ding, Y. W. Wu, I. A. Finneran, L. Anderegg, B. L. Augenbraun, J. M. Doyle, and J. Ye, Phys. Rev. Lett. **121**, 213201 (2018).

84 J. Luque, and D. R. Crosley, LIFBASE: Database and spectral simulation for diatomic molecules, Version 1.6, SRI International (1999).

85 M. E. King, G. M. Nathanson, M. A. Hanninglee, and T. K. Minton, Phys. Rev. Lett. **70**, 1026 (1993).

86 D. J. Garton, T. K. Minton, M. Alagia, N. Balucani, P. Casavecchia, and G. G. Volpi, J. Chem. Phys. **112**, 5975 (2000).

87 J. M. Zhang, D. J. Garton, and T. K. Minton, J. Chem. Phys. **117**, 6239 (2002).

88 J. M. Zhang, H. P. Upadhyaya, A. L. Brunsvold, and T. K. Minton, J. Phys. Chem. B **110**, 12500 (2006).

89 B. C. Marshall, E. J. Smoll, S. M. Purcell, M. L. Costen, K. G. McKendrick, and T. K. Minton, J. Phys. Chem. C **120**, 12472 (2016).

90 M. E. King, K. M. Fiehrer, G. M. Nathanson, and T. K. Minton, J. Phys. Chem. A **101**, 6556 (1997).

91 M. E. King, M. E. Saecker, and G. M. Nathanson, J. Chem. Phys. **101**, 2539 (1994).

92 G. M. Nathanson, P. Davidovits, D. R. Worsnop, and C. E. Kolb, J. Phys. Chem. **100**, 13007 (1996).

93 W. A. Alexander, J. Zhang, V. J. Murray, G. M. Nathanson, and T. K. Minton, Faraday Discuss. **157**, 355 (2012).

94 S. P. K. Kohler, S. K. Reed, R. E. Westacott, and K. G. McKendrick, J. Phys. Chem. B **110**, 11717 (2006).

95 D. Kim, and G. C. Schatz, J. Phys. Chem. A **111**, 5019 (2007).

96 M. Nakauchi, T. Mabuchi, Y. Yoshimoto, T. Hori, I. Kinefuchi, H. Takeuchi, and T. Tokumasu, J. Phys. Chem. C **123**, 7125 (2019).

97 S. R. Cohen, R. Naaman, and J. Sagiv, J. Chem. Phys. **88**, 2757 (1988).

98 A. J. Kenyon, A. J. McCaffery, C. M. Quintella, and M. D. Zidan, J. Chem. Soc. Faraday Trans. **89**, 3877 (1993).